Studies on post-dryout heat transfer in R-134a vertical flow

Ludwig Köckert [*], Aurelian F. Badea, Xu Cheng, Dali Yu, Denis Klingel

Institute of Applied Thermofluidics (IATF), Karlsruhe Institute of Technology (KIT), Kaiserstraße 12, 76131 Karlsruhe, Germany

ARTICLE INFO

ABSTRACT

An experimental study of post-dryout heat transfer with the coolant R-134a was performed in a vertical round tube with upward flow. The experiments were conducted in an uniformly heated tube with an inside diameter of 10 mm and a heated length of 3100 mm, at pressures of 11.1 bar, 16 bar and 28 bar, with varying mass flux in the range of 300–1500 kg/m²s.

The results show that for higher mass fluxes and higher heat fluxes the wall temperature decreases after reaching a peak close to the critical vapor quality, while at lower mass fluxes the wall temperature keeps increasing after dryout. The phenomenon described last is shifted to even lower mass fluxes with rising pressure. Furthermore, it was found that at increasing pressure as well as at increasing mass flux the dryout location is shifted to lower equilibrium vapor qualities.

Based on the experimental results and existing prediction methods, a theoretical model was developed to describe the heat transfer in the post-dryout area. It divides the post-dryout area into a developing and a developed region. A correction factor was introduced to model the droplet distribution in the cross-section of the fully developed region. A comparison with selected post-dryout heat transfer models from the literature for the experimental parameter range in the present study shows a good applicability of the new model.

1. Introduction

Dryout marks the point where in boiling fluid flows the heated surface is not wetted any longer by liquid but instead there is a direct and permanent contact of the heated surface with vapor [1]. The area downstream of the dryout location is denoted as post-dryout (PDO) region; it can be divided into a developing region and a fully developed region. In this approach the fully developed region marks the area in which a stable and continuous vapor phase has been established at the heated wall [2]. At the point of dryout, the flow regime changes from annular two-phase flow to dispersed two-phase flow with liquid droplets entrained in vapor [3,4]. Three mechanisms characterize the heat transfer in the post-dryout area; i) convective heat transfer from wall to vapor and from vapor to liquid droplets, ii) direct heat transfer from wall to droplets and iii) thermal radiation. The last mechanism is often neglected in the literature due to its small magnitude at low wall temperatures [5]. A thermal non-equilibrium between the vapor and the liquid phase - increasing with decreasing mass flux, according to Groeneveld and Delorme [1,4] - is characteristic for the post-dryout area. At the point of dryout a strong rise of the surface temperature can be observed. The downstream temperature distribution in the post-dryout

area depends on different factors, e.g. mass flux, heat flux or pressure.

The phenomenon of dryout occurs e.g. in steam generators or in refrigeration engineering [3]. It is also of great importance in the field of safety in light water cooled nuclear reactors, e.g. in case of a loss of coolant accident. A comprehensive understanding of the heat transfer mechanisms and the temperature distribution in the post-dryout area is therefore fundamental. Numerous experiments on post-dryout heat transfer in different fluids have been conducted and different models to predict the post-dryout heat transfer coefficient (HTC) and therewith the wall temperature have been developed. Experimental research of the post-dryout heat transfer is often performed with refrigerants instead of water since similar phenomena can be observed at lower temperatures and pressures [6]. For practical use in the reactor safety analysis however, the gathered data need to be scaled to water with the help of fluid-to-fluid scaling laws.

Bennett et al. performed steady-state post-dryout and rewetting experiments in different uniformly heated tubes with water [7]. They found that at the onset of dryout the wall temperature steeply increases. The temperature distribution in the post-dryout area depends on the mass flux leading to further increasing wall temperatures at low mass fluxes, slowly increasing or constant wall temperatures at medium mass fluxes and decreasing wall temperatures at high mass fluxes after

---

Nomenclature

d	droplet diameter [mm]	Re	Reynolds number [−]
D	tube diameter [mm]	Pr	Prandtl number [−]
h	enthalpy [J kg^{-1}]		
i_{vd}	latent heat of vaporization [J kg^{-1}]	*Subscripts*	
I	current [A]	-	means "between"
k	thermal conductivity [W m^{-1} K^{-1}]	1	developing region
K_1	correction factor [−]	2	fully developed region
K_2	correction factor [−]	b	bulk
L	length [mm]	d	droplets
$\dot{m}$	mass flow rate [kg s^{-1}]	do	dryout point
p	pressure [bar]	e	equilibrium
$\dot{q}$	heat flux [W m^{-2}]	H	heated
$\dot{Q}$	heat flow [W]	i	inner
$\dot{q}_V$	volumetric heat flux [W m^{-3}]	in	inlet
T	temperature [°C]	ls	liquid at the saturation temperature
U	Voltage [V]	L	loss
v_d	droplet deposition velocity [m s^{-1}]	NB	nucleate boiling
x	vapor quality [−]	o	outer
z	relative length [−]	out	outlet
		sat	saturation
Greek Symbols		sub	subcooled
α	heat transfer coefficient [W m^{-2} K^{-1}]	T	tube
α_{vo}	void fraction [−]	v	vapor
β_1	parameter [−]	vb	vapor at bulk temperature
β_2	parameter [−]	ve	vapor in equilibrium flow
β_3	constant coefficient [−]	vc	vapor in the central region
ε	effectiveness [−]	vf	vapor in the film region
μ	dynamic viscosity [kg m^{-1} s^{-1}]	vs	vapor at the saturation temperature
ρ	density [kg m^{-3}]	vw	vapor at wall temperature
		w	wall

reaching a local maximum. With increasing heat flux the maximum temperature rises while the onset location of critical heat flux (CHF) is shifted upstream. Another comprehensive experimental study of the post-dryout heat transfer in water using uniformly heated round tubes with different inner diameters was done by Becker et al. with a broad range of experimental parameters [8]. Their results confirmed the general temperature distributions for low and high mass flux (this aspect will be referred in detail also by this work in Subsection 3.1). Both tendencies are pronounced with decreasing and increasing mass flux, respectively, according to Becker et al. [8]. Nishikawa et al. confirmed the general temperature distributions and the tendencies regarding the onset of CHF found in water for low and high mass flux also for the coolant R-22 [9]. Lee and Chang [10] found the same temperature distribution for high mass fluxes in their experiments with R-134a as well. They also investigated the influence of increasing pressure on the post-dryout temperature distribution. It was observed that increasing pressure leads to a maximum wall temperature decrease for lower mass fluxes. Furthermore, increasing pressure pronounces the shift of the critical vapor quality to lower values when the heat flux increases as well. Schnittger also detected the critical vapor quality shift with increasing pressure in his experiments with R-12 [5]. According to his studies, this shift can also be observed when increasing the mass flux. However, increasing pressure does not significantly change the location of the dryout onset. In the post-dryout area, the temperature keeps increasing for lower pressures while it decreases at higher pressure with a steeper reduction for increasing pressure. Schnittger also found that with increasing mass flux, the temperature rise at the point of dryout decreases. The tendencies regarding the dryout location as well as the temperature distribution in the post-dryout area are relatively similar to the ones with increasing pressure. Increased heat flux leads to overall higher wall temperatures while the slope remains almost the same in the

post-dryout area.

Most of the above-mentioned authors used their experimental results to develop different kinds of post-dryout heat transfer correlations and models which are mainly limited to the range of their experimental parameters [5,7,9–11].

Besides the foregoing experimental work and derived theoretical models, numerous further works have been conducted regarding the development of prediction methods to describe the post-dryout heat transfer. Excellent reviews of these modeling works could be found in articles [4,12,13]. Different types of models and correlations have been developed and were applied with varying degree of success. These works can be classified as correlative works and analytical works. Most of the proposed correlative works are based on a single-phase wall-vapor convective heat transfer correlation. In this correlation the coefficients are usually modified to account for the impact of dispersed droplets on the convection. In most of the analytical works on the other hand the prediction of the wall temperature is attempted by considering three-path heat transfer which involves the following heat transfer mechanisms: i) heat transfer from the heated wall to vapor, ii) heat transfer from vapor to droplets, iii) heat transfer from wall to droplets, including direct contact of wall and droplets and thermal radiation. Generally, a one-dimensional separated flow model is used in many early-stage investigations [14–18]. The only difference can be found in the selection of empirical correlations for convective and interfacial heat transfer or in the selection of droplet size calculation models.

In recent years, a computational fluid dynamics (CFD) approach has been employed to capture more detailed phenomena ([19–23]), among others the vapor-droplet interface, the droplet concentration distribution as well as local vapor superheat. Further works to predict dryout and post-dryout behavior have been carried out by Li and Anglart [24] as well as by Shi et al. [25], accounting for droplet behavior at and

beyond dryout or for the liquid film propagation on solid walls.

An analytical model was developed for the whole post-dryout region in previous works by the authors [2,26]. The model was developed for experiments with water. In that model, the fully developed region is divided into a film region and a central region to account for the impact of the droplets' volumetric concentration on the interfacial heat transfer between vapor and droplets. The comparison with some experimental data indicates that the developed model could provide a satisfying agreement in the prediction of the post-dryout heat transfer.

The introduced experiments as well as the post-dryout heat transfer models and correlations have in common that they are often limited to relatively narrow geometrical boundary conditions and parameter combinations regarding e.g. mass flux, pressure or heat flux. Especially the number of available post-dryout heat transfer data with the fluid R-134a is currently still very limited. Therefore, further experimental research is necessary to enhance the existing data base in R-134a and to gain a comprehensive understanding of the heat transfer mechanisms and the temperature distribution in the post-dryout area. The Becker data base [8] was used to derive the parameter range for the experiments. In addition to extending the currently existing data base those experimental data provide also a data base for the improvement of a fluid-to-fluid scaling law developed at the KIT. Since the currently available theoretical models are not able to predict the temperature distribution in the post-dryout region for a wide range of parameters or different fluids further development in the field of modeling is needed as well.

In this study, steady-state post-dryout heat transfer experiments in a uniformly heated round tube using the coolant R-134a were conducted. The general temperature distribution as well as the influence of heat flux, mass flux and pressure are analyzed. The experimental results support the improvement of the authors' theoretical model that considers the heat transfer mechanistic features, e.g. the thermal non-equilibrium and the droplet behavior in the post-dryout region and therefore allows the prediction of wall temperature development in this area for a broader parameter range than the currently available models.

2. Experimental facility and measurement method

2.1. Experimental facility

An experimental study of the post-dryout heat transfer was performed at the KIT Model Fluid Facility (KIMOF). The set-up of the facility is schematically shown in Fig. 1 a). The refrigerant R-134 was used as working fluid.

The fluid circulates in the main loop via the coolant pump. After leaving the pump it passes a pre-heater which allows to set up a stable inlet temperature at the entrance of the test section. The set-up of the test section where the actual heat transfer measurements take place is shown in Fig. 1 b) and will be described later. The fluid passes two heat exchangers after leaving the test section of which the first one operates on cooled water via a cooling tower. The second one is fed by a cooling machine.

The mass flux is measured via a Coriolis mass flow meter. The pressurizer operates on hydraulic oil. It regulates the system pressure and furthermore helps to mitigate pressure fluctuations in the main loop. The entire system is run and controlled with the help of a Wago control system. Together with 3 data loggers it delivers all relevant measurement parameters which can be displayed and saved via the software LabVIEW.

2.2. Test section

The test section consists of a tube with an inner diameter of 10 mm and an outer diameter of 12 mm and is installed vertically. It is made of the austenitic steel X5CrNi18-10 and is heat resistant until 550 °C. The fluid in the test section flows vertically upward. To heat up the test section there are two current connectors within a distance of 3100 mm. For heating purposes, DC is uniformly delivered by a transformer. The rest of the loop is electrically isolated from the test section with two isolation flanges. Along the heated length the outside wall temperature is measured with 55 type-T thermocouples. They are mounted on to the wall on opposite wall sides starting on the left side 138 mm above the lower current connector as can be seen in Fig. 1 b). The longitudinal distance between thermocouples is 60 mm. Every ten thermocouples
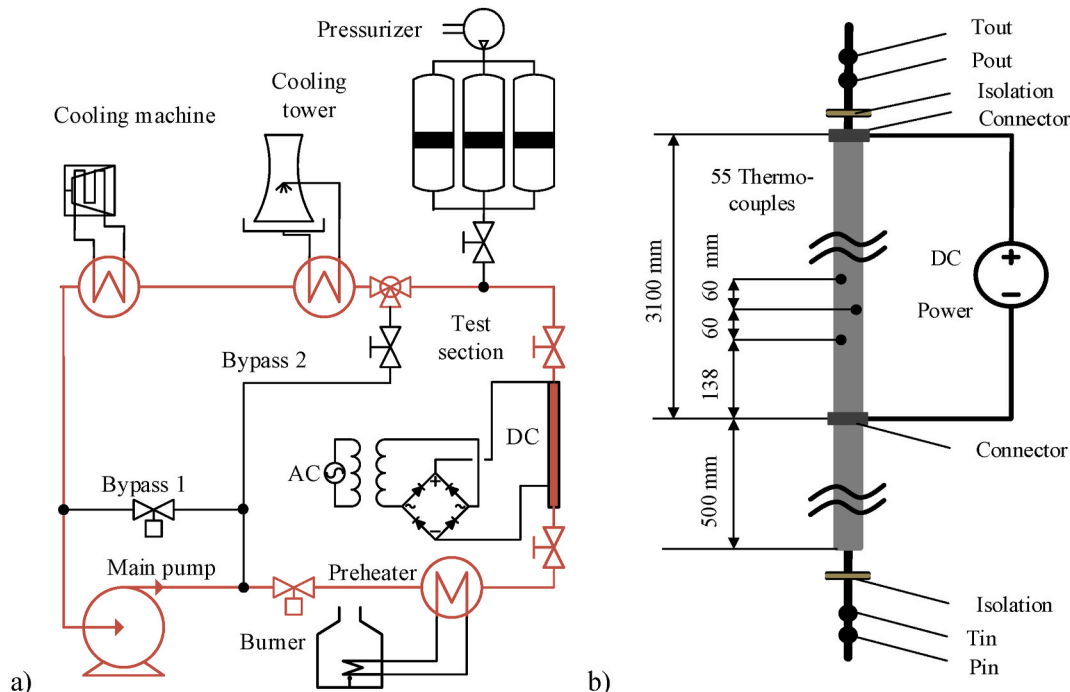
Fig. 1. Schematic set-up of a) the KIMOF test facility, b) the test section.

starting from thermocouple 12 and 13, two thermocouples are mounted on the same height on opposite sides of the wall.

The fluid temperature is measured at the inlet and the outlet of the test section with type-T in-stream thermocouples. Besides the temperature, the pressure at the inlet and outlet is measured as well.

The entrance length of the test section is 500 mm to guarantee a fully developed flow at the beginning of the heated length.

Two layers of mineral wool with an overall thickness of 50 mm thermally insulate the test section against the environmental conditions.

2.3. Experimental procedure and test data reduction

The post-dryout experiments were carried out as steady-state experiments. At constant pressure, inlet temperature and mass flux, the heat flux was increased in pre-defined steps of 5 kW/m^2. The test matrix is shown in Table 1 with the pressures for R-134a and the equivalent in water.

The average heat flux can be described as follows:

$$\dot{q} = \frac{UI - \dot{Q}_L}{\pi \, L_H \, D_i} \tag{1}$$

with the product of the voltage U and the current I defining the electrical power. The heat loss is described by $\dot{Q}_L$, the heated length by L_H and the inner diameter by D_i.

By stepwise increase of the heat flux the wall temperatures increase as well until dryout occurs at the end of the heated length. The onset point of dryout is moving upstream with further increase of the heat flux. The post-dryout area lies downstream of the onset point of dryout. Measurements were taken after all the parameters reached steady-state. Every measurement took 60 s. For analyzing the results, the mean value of this 60 s measurement was taken. The maximum outer wall temperature was limited to 240 °C to avoid thermal instability and decomposition (including gas release) of the working fluid as this could lead to different operation conditions and physical affectation of the facility depending on the amount of gaseous and solid decomposition products. This subsequently limits the maximum heat flux (further also referred to as the highest admissible heat flux).

The parameters in the experiments were kept within certain tolerance ranges. The deviation of the mass flux was kept within 2% of the prescribed value. The tolerance for the pressure was ±0.3 bar while the tolerance for the heat flux and the test section inlet temperature was within ±0.5 kW/m^2 and ±0.5 °C, respectively.

In the analysis of the experimental results instead of the measured outer wall temperature, the inner wall temperature was used. The inner wall temperature was calculated for the simplified case of one dimensional heat conduction as follows:

$$T_{w,i} = T_{w,o} - \left(\frac{\dot{q}_V}{16\,k}\right)(D_i^2 - D_o^2) + \frac{D_o}{2\,k}\left[\left(\frac{\dot{q}_V\,D_o}{4} - \dot{q}_L\right)\log\left(\frac{D_i}{D_o}\right)\right] \tag{2}$$

$T_{w,o}$ describes the outer wall temperature while D_o and D_i represent the

outer and inner diameters of the tube and k stands for the thermal conductivity.

The volumetric heat flux for round tube geometries $\dot{q}_V$ and the heat loss at the outer wall $\dot{q}_L$ are calculated as follows:

$$\dot{q}_V = \frac{UI}{\frac{\pi}{4}\,L_H\,\left(D_o^2 - D_i^2\right)} \tag{3}$$

$$\dot{q}_L = \frac{\dot{Q}_L}{\pi\,L_H\,D_o} \tag{4}$$

The heat loss power $\dot{Q}_L$ was determined in experiments with an evacuated test section which means that vacuum conditions were set in the thermally insulated test section. In the following diagrams the equilibrium quality is used which is described as below:

$$x_e = \frac{h - h_{ls}}{h_{vs} - h_{ls}} \tag{5}$$

with the enthalpy h at the point of interest and the enthalpies h_{ls} and h_{vs} at the liquid and the vapor saturation point, respectively.

The enthalpy at the point of interest is given by the simplified first law of thermodynamics:

$$h(z) = h_{in} + z\,\frac{\dot{Q}}{\dot{m}} \tag{6}$$

with the inlet enthalpy h_{in}, the heat flow $\dot{Q}$ and the mass flow rate $\dot{m}$. The relative length z is given by the ratio of the distance between the point of interest and the start of the heated length L to the overall heated length L_H:

$$z = \frac{L}{L_H} \tag{7}$$

The fluid enthalpy at the point of interest in combination with the pressure in the test section helps to extract the fluid bulk temperature T_b out of the data bank of the National Institute of Standards and Technology (NIST).

2.4. Measurement uncertainties

Before the actual post-dryout experiments, single phase flow experiments to determine the heat balance and experiments for the heat loss of the test section were conducted.

The heat balance between measured and calculated enthalpy over the test section delivered an average deviation of 2.03%.

The instrumentation to measure the parameters relevant for the heat transfer analysis was carefully checked beforehand. The corresponding uncertainties of the instrumentation as well as of the test section geometry are given by the manufacturers and are listed in Table 2.

Several test runs were repeated to investigate the reproducibility of the experiments. Table 3 shows the test matrix of the repeated test runs. Overall, the test runs show a good reproducibility of the initial experiments, within an average deviation range of 2–6%.

3. Experimental results and discussion

3.1. General temperature distributions

Two general temperature distributions (types I and II, to be

Table 1
Experimental parameters.

Pressure [bar]		T_{sat}-T_{in} [°C]	Mass flux [kg/m^{2}s]	Heat flux [kW/m^2]
R-134a	Water			
11.1	69.1	10	300, 500, 700, 900, 1100, 1300, 1500	40–140
16	97.4	10	300, 500, 700, 900, 1100, 1300, 1500	30–120
28	161.6	10	500, 700, 900, 1100, 1300, 1500	30–85
28	161.6	15	300	20–50

Table 2
Parameters and their manufacturing uncertainties.

T_{in}, T_{out}, $T_{w,o}$	p	Voltage	Current	Mass flow	D_i	D_o
0.4% or 0.5 °C	0.25%	0.03%	2%	0.05%	0.03 mm	0.05 mm

Table 3
Test matrix of the reproducibility experiments.

Pressure [bar]	T_{sat}-T_{in} [°C]	Mass flux [kg/m²s]	Heat flux [kW/m²]
11.1	10	500	55–90
		1500	85–140
16	10	900	50–105
		1500	70–115
28	10	1100	40–80
		1500	50–85

explained next) were found in the steady-state experiments of the post-dryout heat transfer. They mainly depend on the mass flux and the heat flux. The two different temperature distributions can be observed in Fig. 2. The diagrams in Fig. 2 show the difference between the inner wall temperature and the saturation temperature versus the equilibrium vapor quality. Equilibrium vapor qualities below 0 correspond to sub-cooled liquid while qualities above 1 to superheated vapor flows, respectively. It is worth mentioning that the temperature distributions seem to follow a certain zig-zag pattern which is presumably caused by an eccentricity of the heated tube.

At the inlet of the test section the fluid is subcooled as can be seen in the test matrix in Table 1. When CHF is reached, dryout occurs which leads to a sudden and steep increase of the wall temperature due to a sudden drop of the heat-transfer coefficient in succession of the flow regime change. The corresponding vapor quality is called critical vapor quality.

At low mass flux and low heat flux (type I) the wall temperature keeps increasing in the post-dryout area as can be observed in Fig. 2 a). Although the slope is less steep than at the point of dryout, it always remains positive thus leading to continuously increasing wall temperatures with increasing vapor quality.

In Fig. 2 b) the characteristic post-dryout temperature distribution for high mass flux and high heat flux (type II) is shown. At first, the wall temperature keeps increasing in the post-dryout area with a less steep slope than at the onset of dryout. After reaching a local maximum the temperature decreases with increasing vapor quality. Other experimental work [8,9] show that at vapor qualities higher than 1 the temperature increases again. This temperature development is well described in the literature [3,4]. Near the point of dryout most of the heat transferred from the wall to the fluid is used to superheat the vapor. At a certain distance from the point of dryout the heat transfer from vapor to droplets increases leading to a higher evaporation rate and therefore higher vapor acceleration. This slows down the temperature increase or even leads to a temperature decrease at high mass fluxes. The decrease of the temperature at high mass fluxes can be explained by the lower equilibrium vapor quality in comparison to lower mass fluxes (see Subsection 3.3) which leads to a higher evaporation rate in the post-dryout region and therefore higher vapor acceleration. Starting at a certain vapor quality, the temperature increases again due to the decreasing droplet surface and thus lower evaporation rate which leads

to vapor superheating. Such high vapor qualities could not be reached for high mass fluxes in the present experiments due to the overall temperature limitation of 240 °C.

The observations are in an overall good agreement with the reviewed literature in the introduction. They are valid for all the different fluids investigated [5,7–9]. Furthermore, the two characteristic temperature distributions are in line with the assumption made in the literature [1,4] that with increasing mass flux the thermal non-equilibrium decreases. This assumption is explainable with the increasing turbulence of the flow at increasing mass flux which leads to lower equilibrium qualities and therefore a bigger liquid portion in the flow. The overall droplet surface increases with increasing liquid portion in the flow, leading to a better heat transfer through evaporation and therefore to a decreasing thermal non-equilibrium.

3.2. Influence of heat flux

The variation of the heat flux at otherwise constant parameters is shown in Fig. 3 for high and for low mass flux. As can be seen for high mass fluxes in the range of 1500–1100 kg/m²s (depending on the pressure of which the influence is described in Subsection 3.4), high heat flux has 2 effects: i) with increasing heat flux the sudden temperature rise at the onset of dryout increases as well as the overall maximum wall temperatures, ii) increasing heat flux leads to a shift of the critical vapor quality to lower values (see Fig. 3 a)).

With lower mass flux, the first observation can be confirmed while the effect of the shift of the vapor quality to lower values diminishes and cannot be observed anymore at very low mass fluxes (see Fig. 3 b)).

Since the heat transfer from wall to vapor is less effective than the heat transfer from wall to liquid, the heat transfer coefficient drops at the point of dryout, leading to higher wall temperatures. This phenomenon is pronounced with increasing heat flux and therefore explains the first observation.

The phenomenon observed in Fig. 3 a) (at high mass flux) is possibly caused by a combination of the increased heat flux and the higher turbulence at high mass flow rate. The increased heat flux shortens the annular flow length. This effect should be more pronounced at high mass flux, where the high flow velocities may cause a thinner liquid layer leading to an even quicker dryout at lower critical vapor qualities.

3.3. Influence of mass flux

Since the necessary heat fluxes to reach dryout and the admissible maximum wall temperature strongly depend on pressure and mass flux, it is impossible to have test data with all different mass fluxes and the same values of all other parameters.

As can be observed in Fig. 4a), for higher mass fluxes the characteristic temperature distribution for high mass flux and high heat flux is shown at all the different mass fluxes. After reaching the local maximum, the wall temperatures decrease again due to increased

a) b)
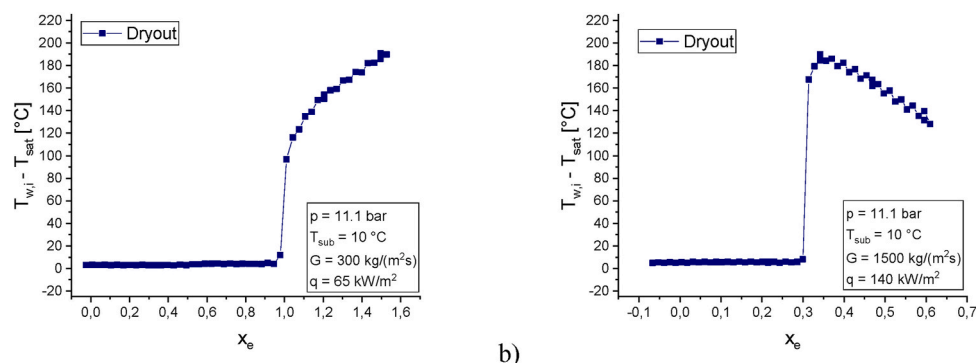
Fig. 2. Characteristic temperature distribution at a) low mass flux and low heat flux, b) high mass flux and high heat flux.
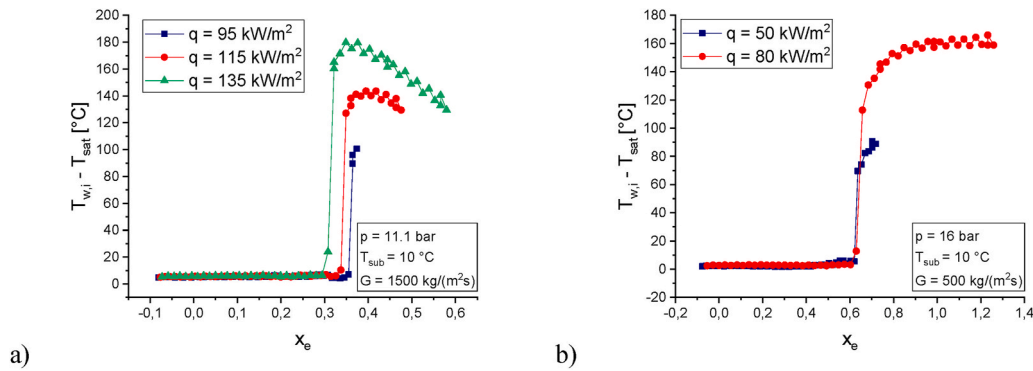
Fig. 3. Influence of the heat flux on the temperature distribution at a) high mass flux, b) low mass flux.
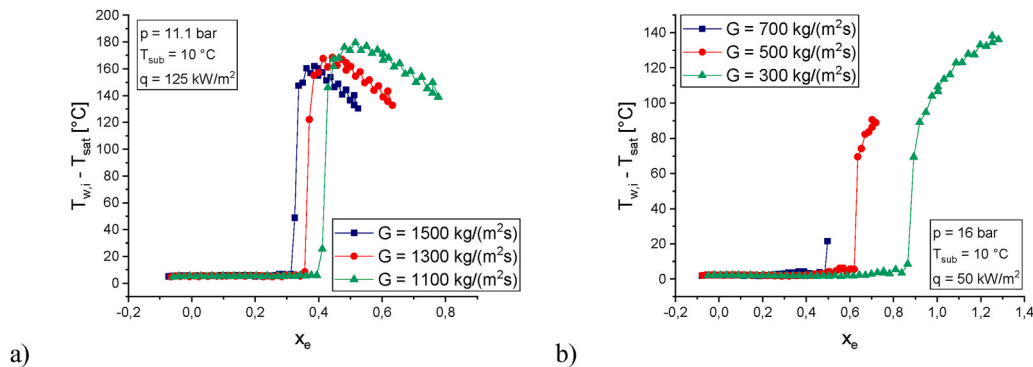
Fig. 4. Influence of the mass flux on the temperature distribution at a) higher mass fluxes, b) lower mass fluxes.

evaporation of the entrained droplets and hence vapor acceleration which leads to a better convective heat transfer [3,10]. With increasing mass flux, the critical vapor quality is shifted to lower values. This phenomenon is called inverse mass flux effect and was described by Tong and Tang [27]. The lower vapor quality in the PDO region with increasing mass flux is caused by the higher turbulence in the fluid flow, as described in Subsection 3.1. Furthermore, it is remarkable that with increasing mass flux, the temperature rise at the point of dryout decreases, which can be explained by the improved convective heat transfer with higher flow velocity. The slope of the temperature decrease in the post-dryout area is very similar for all mass fluxes, although the overall temperature is higher for lower mass fluxes.

For lower mass fluxes the typical temperature distribution of the type I can be observed (see Fig. 4 b)). After the steep temperature increase at the critical vapor quality the wall temperatures keep increasing in the post-dryout area with a less steep slope. With decreasing mass flux, the critical vapor quality and the temperature increase at the onset of dryout rise due to the lower vapor velocity.

In the conducted experiments, the necessary heat flux to reach CHF as well as the maximum heat flux increase with increasing mass flux. The reason for this phenomenon is the improved convective heat transfer at higher flow velocities. This relationship is only valid to a certain vapor quality. Generally speaking, CHF increases linearly with decreasing critical vapor quality [28]. While at low critical vapor qualities increasing mass flux leads to higher flow turbulence and therefore higher CHF, this dependence changes with increasing vapor quality, so that increasing mass flux decreases CHF (inverse mass flux effect [27]).

3.4. Influence of pressure

When investigating the influence of the pressure similar difficulties as with the mass flux occur. Therefore, there is just a very limited number of examples where the whole pressure range can be observed

while all the other parameters are the same.

As Table 4 shows for two exemplary mass fluxes, the minimum heat flux, which marks the necessary heat flux to reach CHF, and the maximum heat flux decrease with increasing pressure which can be explained by the decreasing evaporation enthalpy with increasing pressure.

Fig. 5 a) points out that with increasing pressure the critical vapor quality is shifted to lower values. The measurement points in the figure are individually delivered by the thermocouples (uniformly distributed) along the test section. One may observe that the dryout location is shifted upstream by increasing pressure (confirmed by the increasing number of thermocouples in the PDO area). This contradicts the statement of Schnittger that the dryout location remains the same with increasing pressure [5]. Furthermore, the temperature rise at the onset of CHF is more pronounced with increasing pressure as well. This might be caused by the higher vapor density at high pressure which leads to a lower vapor velocity.

As mentioned in Subsection 3.1, the pressure also influences the general temperature distribution. The plot in Fig. 5 b) shows the temperature distribution for the mass flux of 500 kg/m²s at the 3 different pressure levels, each with the highest admissible heat flux. Since a quantitative comparison with more than one free variable is impossible, this diagram was used to show the qualitative change in the temperature

Table 4

Comparison of experimental parameters at two different exemplary mass fluxes.

Mass flux [kg/m²s]	T_{sat}-T_{in} [°C]	Pressure [bar]	Heat flux [kW/m²]
1500	10	11.1	90–140
		16	75–120
		28	55–85
500	10	11.1	60–90
		16	45–85
		28	35–65

a)

b)
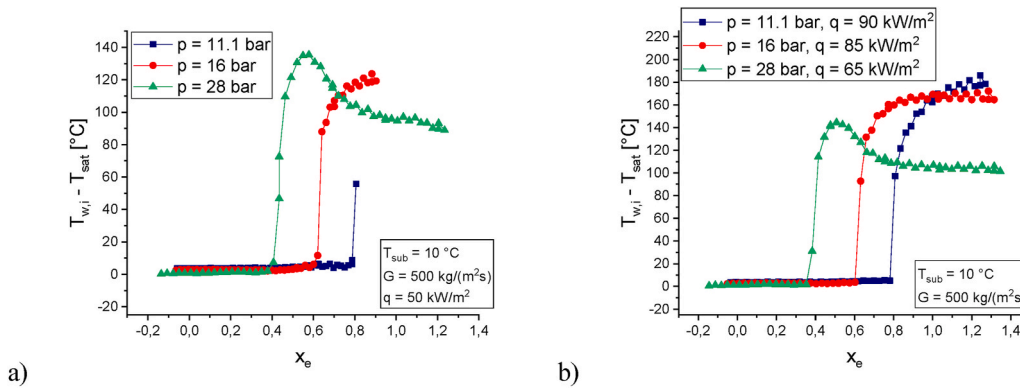
Fig. 5. Influence of the pressure on the temperature distribution at a) constant other parameters, b) the highest admissible heat flux for the given pressures and mass flux.

distribution at different pressures. It is noticeable that for an exemplary, relatively low mass flux of 500 kg/m²s the general temperature distribution changes from type I to type II (defined earlier in section 3.1) with increasing pressure. Schnittger found the same phenomenon in his experiments with the fluid R-12 [5]. A possible explanation for this phenomenon is given by Lee and Chang [10]. With increasing pressure the density ratio $\frac{\rho_l}{\rho_v}$ decreases significantly which leads to a decreasing void fraction. A lower void fraction on the other hand causes a lower vapor superheat and hence a better convective heat transfer through a lower thermal non-equilibrium. Since the thermal non-equilibrium is more pronounced with decreasing mass flux, this effect is more significant for low mass fluxes. Thus, based on the present experimental results, the conclusion can be made that with increasing pressure the transition between the two types of temperature distributions is shifted to lower mass fluxes and heat fluxes.

It is noticeable, that the wall temperature at 28 bar does not rise for vapor qualities above 1. This is explainable with the thermal non-equilibrium in the flow. At thermal equilibrium, all the liquid should be evaporated at $x_e = 1$ and the heat is solely used to superheat the vapor which leads to an increase in wall temperature. In the thermal non-equilibrium flow, entrained liquid droplets even beyond equilibrium vapor qualities of 1 can be found. Cumo et al. even detected droplets up to $x_e = 2.2$ [29]. These droplets enhance the heat transfer through evaporation and might postpone the onset of temperature increase.

4. Post-dryout modeling

4.1. KIT mechanistic model

As mentioned earlier, an analytic model was developed for the whole post-dryout region in a previous work of the authors [2,26,30]. The model considers three paths for heat transfer that involves heat transfer from i) the heated wall to vapor, ii) vapor to droplets, iii) wall to droplets. Liquid droplets are treated as single average sized and the vapor phase is continuous. The distribution of droplets concentration in the cross section is considered, which could greatly affect the heat transfer from vapor to droplets. All kinds of radiative heat transfer are neglected since the focus lies on flow conditions in post-dryout, in which the wall temperature is not as high compared to post-DNB (departure from nucleate boiling) conditions.

This section introduces the basics of the model and puts emphasis on the changes to the previous version of the model. Further specifics can be found in Refs. [2,26,30].

As mentioned in the introduction the model divides the PDO area into a developing and a fully developed region. The latter one is divided again cross-sectionally into a core region in the center of the tube and a film region close to the tube walls.

The convective heat transfer between wall and vapor is considered separately in the different regions. In the developing region, marked with the subscript 1, this heat transfer is regarded as a transient entrance-region problem with axial distance from the dryout location. In the present modeling approach the measured dryout location is used as input to determine the dryout elevation along the tube. The convective heat transfer between wall and vapor in the developing region is therefore expressed as follows:

$$\alpha_{w-v,\,1} = (1 - K_1)\alpha_{w-v,\,2} + K_1\alpha_{NB} \tag{8}$$

where K_1 is a dimensionless correction factor, representing the ratio of the nucleate boiling heat transfer rate to the total heat transfer rate and α_{NB} is the heat transfer coefficient at nucleate boiling conditions.

The convective heat transfer between wall and vapor in the fully developed PDO region, marked as 2, was predicted by the Hadaller correlation [31] in the first version of the model and is described as follows:

$$\alpha_{w-v,\,2} = 0.008348 \frac{k_{vf}}{D_T} Re_{vf}^{0.8774} Pr_{vf}^{0.6112} \tag{9}$$

The Hadaller correlation was developed for water. In the present model the Forslund correlation [32] is utilized to predict the convective heat transfer for R-134a. In the current work, the Forslund correlation is found to deliver good results for R-134a but shows an overestimation when the wall-bulk temperature ratio increases. This is because the influence of lower density and higher viscosity of vapor at high temperatures near the superheated wall is not considered. Conventionally, a correction factor in form of a temperature or a viscosity ratio is multiplied with the convective heat transfer correlation to account for the significant fluid property variations across the tube. In the present model, the latter option combined with a constant coefficient of 1.05 is chosen to model the viscosity variation across the tube cross section. The constant multiplier as well as the exponent of the viscosity ratio are derived by comparison of the model and the experimental data base. Finally, the correlation is proposed:

$$\alpha_{w-v,2} = 0.03675 \frac{k_v}{D_T} Re_v^{0.743} Pr_v^{0.4} \left(\frac{\mu_v}{\mu_{vw}}\right)^{0.1} \tag{10}$$

The heat flux between wall and droplets is calculated by the following equation:

$$\dot{q}_{w-d} = \frac{i_{vd}\, v_d\, \rho_d\, \frac{\beta_1}{\beta_2}\, \varepsilon}{2} \tag{11}$$

in which i_{vd} represents the latent heat of vaporization, v_d the droplet deposition velocity, ρ_d the droplet density; β_1 and β_2 are representing coefficients accounting for the effect of superheat on the vapor temperature profile and ε is the effectiveness parameter.

The interfacial heat transfer between vapor and droplets is based on the Hughmark correlation [33]. While specifics about the derivation can be found in the named literature as well as in Refs. [2,30], the overall interfacial heat flux from vapor to droplets in the authors' model is expressed as follows:

$$\dot{q}_{v-d} = (1 - K_2)\alpha_{v-d, \, vc}(T_{vc} - T_{sat}) + K_2\alpha_{v-d, \, vf}(T_{vf} - T_{sat}) \qquad (12)$$

with $\alpha_{v-d, \, vc}$ and T_{vc} being the heat transfer coefficient from vapor to droplets and the vapor temperature in the central region as well as $\alpha_{v-d, \, vf}$ and T_{vf} in the film region, respectively. The correction factor K_2 is employed by the authors and represents the ratio of droplets' evaporation happening in the film region and the total evaporation. The correlation has the form:

$$K_2 = \beta_3 \, \alpha_{vo}^2 \left(\frac{Re_d}{Re_{vb}}\right)^{1.5} \left(\frac{D_T}{d}\right)(x_e - x_{do})^2 \qquad (13)$$

In the previous model the correlation was solely developed for water and the constant coefficient β_3 was given with 7500. The constant coefficient in the present model is adjusted to 4500 through data fitting on the R-134a database.

4.2. Comparison with test data

For a comparison, all the data points were selected at a criterion of void fraction greater than 0.8 to make sure that the flow conditions of the data points are in the post-dryout region. Only the data points in the fully developed post-dryout region were considered. Finally, a total number of 1820 points from the KIMOF test facility was used.

The heat transfer coefficient is defined as,

$$\alpha = \frac{\dot{q}_w}{T_w - T_{ve}} \qquad (14)$$

Fig. 6 compares the predicted HTCs with the measured ones. It shows that on average the present model over-predicts the experimental data by 7.99% with an RMS error of 11.07%. The error is defined as the ratio of the difference between the predicted and the measured heat transfer coefficient to the measured one.

A few well-known models were also selected, including Groeneveld's model [1], the CSO model [34], Yoder's model [18] and the modified Dougall-Rohsenow's model [35], and compared with the test data from the KIMOF test facility. While the first 3 mentioned models are empirical non-equilibrium models, the modified Dougall-Rohsenow model describes an equilibrium correlation to model the wall-to-vapor heat
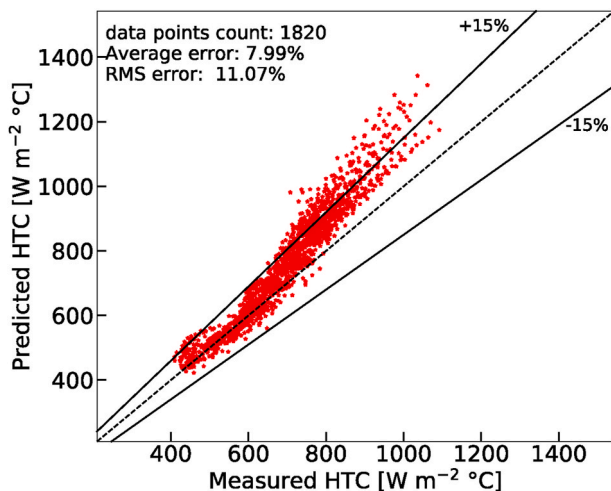
transfer in the PDO area. All the comparison results are summarized in Table 5. Yoder's model applies several empirical correction factors on the convective heat transfer correlation, which improve the prediction for water but over-predict the results for R-134a significantly. The modified Dougall-Rohsenow's model underestimates the wall temperature since the model did not account for the vapor non-equilibrium. The present model obviously gives the best prediction for the test data from R-134a.

A comparison has been done between those experimental tests investigating the influence of heat flux, mass flux and pressure and the present model. Fig. 7 shows that the model is able to capture well the wall superheat profile in PDO for the influences of a) heat flux, b) pressure and c) mass flux. Nonetheless, it has the tendency to underestimate the magnitude of the temperature profile in the PDO area, especially for low quality flow. In this case the model tends to overestimate the wall-vapor convective heat transfer enhancement, caused by the droplets in the fully developed PDO area [30]. This is obvious in Fig. 7 b) for a high pressure of 28 bar and high mass flux at which flow quality and thermal non-equilibrium are assumed to be low.

4.3. Further model development

The here recalled mechanistic model is partially based on flow mechanics and behavior. To verify and possibly enhance this model, additional knowledge - especially about the droplet behavior such as droplet distribution, direction, size and velocity in the PDO area - is needed.

To gain this necessary information, an annular test section with 3 modules was developed and integrated into the KIMOF test facility, granting optical access to one module along the flow channel. The annular set-up is supposed to deliver valid information about the flow behavior in the post-dryout area, helping to verify and enhance the heat transfer (mechanistic) model. As displayed by Fig. 8 a), one of the modules carries 32 bull's eye shaped windows on opposite channel walls, 16 along each wall side. They have a 25 mm diameter field of vision and are manufactured from borosilicate. In the center of the square channel there is a directly heated circular tube made of X5CrNi18-10. The high-speed camera used for the current experimental investigations is a Sprinter-FHD manufactured by the Optronis GmbH. The minimum exposure time of the camera lies at 4 μs. Fig. 8 b) exemplary displays a footage of a dispersed vertical R-134a flow, as taken with the described camera system. It shows the flow channel with the heating circular tube in the middle.

In addition, appropriate options are foreseen for the integration of an optical fiber measurement system into the flow channel. With the optical fiber it is intended to measure the actual vapor temperature and therewith precisely account for the thermal non-equilibrium in the introduced model.

5. Conclusions

Steady-state post-dryout heat transfer experiments at the KIMOF test facility were carried out over a wide parameter range in a uniformly heated round tube with the coolant R-134a as fluid. Furthermore, a

Fig. 6. Heat transfer coefficient comparison between the present model and the experimental data from the KIMOF test facility.

Table 5
Comparison results of HTC predictions between various models and correlations, and the test data from the KIMOF test facility.

	Groeneveld, 1976	CSO, 1979	Yoder, 1982	Dougall-Rohsenow, 1975	KIT model
Average error [%]	31.17	−15.7	58	152	7.99
RMS error [%]	48.40	46.28	61	360	11.07
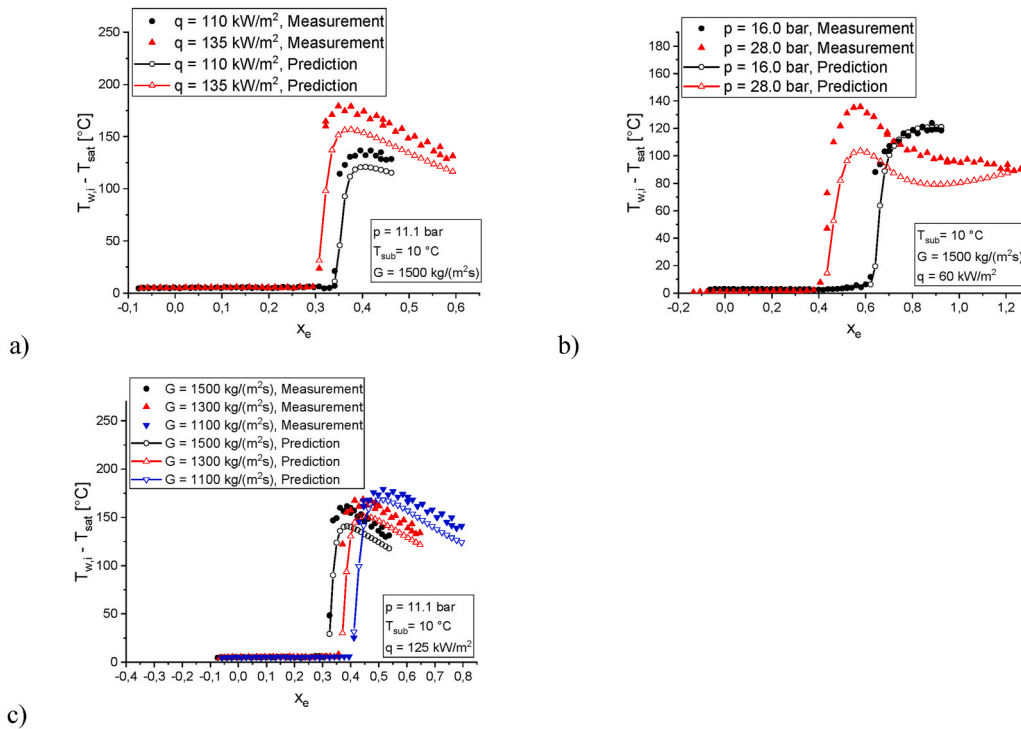
Fig. 7. a) Influence of the heat flux on the temperature distribution at high mass flux, b) Influence of the pressure on the temperature distribution at constant other parameters, c) Influence of the mass flux on the temperature distribution at higher mass fluxes.
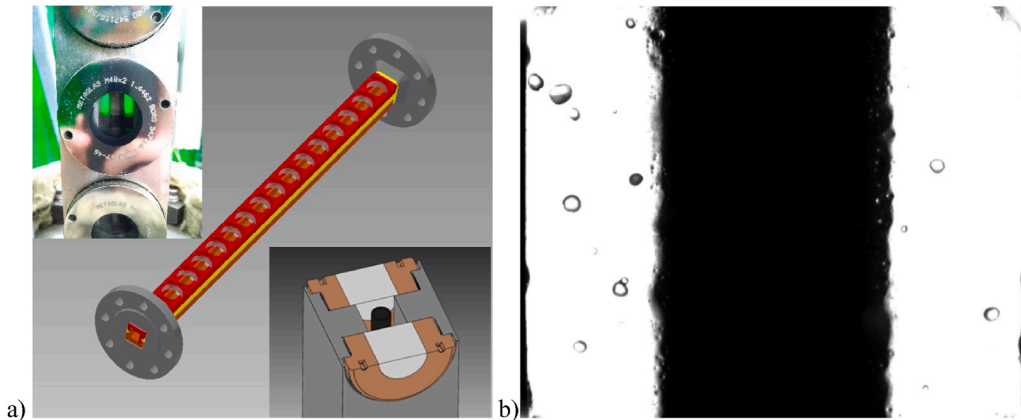
Fig. 8. a) New test section with 32 bull's eye shaped windows on opposite channel walls (lower corner: its cross section with the heating tube in the center of the square flow channel; upper corner: one of the bull's eyes with the heating tube in the center), b) High-speed camera footage of dispersed flow at p = 9.8 bar, G = 61 kg/(m² s), T_{sub} = 16 °C.

previous post-dryout heat transfer (mechanistic) model proposed for water was extended to R-134a. The main results achieved are summarized as follows:

1. Two characteristic post-dryout temperature distributions (types I and II) were experimentally found. When reaching CHF, the temperature increases steeply and suddenly. At low mass fluxes and low heat fluxes the temperature keeps increasing in the post-dryout area with a slope less steep (type I). At high mass fluxes and high heat fluxes the wall temperature reaches a local maximum and decreases again with increasing vapor quality (type II).

2. Increasing heat flux leads to a stronger temperature increase at the onset of dryout and higher maximum wall temperatures.

3. Increasing mass flux shifts the critical vapor quality to lower values. Furthermore, at high mass fluxes increasing heat flux leads to a shift

of the critical vapor quality to lower values as well, being not the case for low mass flux. Decreasing mass flux leads to higher temperature increase at the onset of dryout. The heat fluxes which correspond to the onset of dryout and to the admissible maximum wall temperature decrease with decreasing mass flux.

4. Increasing pressure leads to lower heat fluxes and lower critical vapor qualities while the temperature rise at CHF is pronounced. With increasing pressure, the transition from temperature distribution type I to type II occurs at lower mass flux.

5. Comparison of the mechanistic model with 1820 data points in R-134a at a dryout void fraction higher than 0.8 gives an average error of 7.99% and an RMS error of 11.07%. In comparison to other selected post-dryout heat transfer models, the current model shows the best agreement with the experimental data. In addition, the wall temperature distribution in the PDO region is predicted well for the

effects of heat flux, mass flux and pressure. Especially for low quality flow, the model tends to underestimate the magnitude of the temperature profile.

6. To verify and possibly enhance this model, additional knowledge - especially about the droplet behavior such as droplet distribution, direction, size and velocity in the PDO area - will be acquired out of more detailed experiments.

Declaration of competing interest

The authors declare that they have no known competing financial interests or personal relationships that could have appeared to influence the work reported in this paper.

Acknowledgments

References

[1] D.C. Groeneveld, G.G.J. Delorme, Prediction of thermal non-equilibrium in the post-dryout regime, Nucl. Eng. Des. 36 (1976) 17–26.

[2] D. Yu, F. Feuerstein, L. Koeckert, X. Cheng, Analysis and modeling of post-dryout heat transfer in upward vertical flow, Ann. Nucl. Energy 115 (2018) 186–194.

[3] Vdi-Gvc, publisher, VDI-wärmeatlas, Chapter H3.5 and H3.6, Springer Vieweg, Berlin Heidelberg, 2013.

[4] D.C. Groeneveld, Post-dryout heat transfer: physical mechanisms and a survey of prediction methods, Nucl. Eng. Des. 32 (1975) 283–294.

[5] R.B. Schnittger, Untersuchungen zum Wärmeübergang bei vertikalen und horizontalen Rohrströmungen im post-dryout Bereich, Diss, University, Hannover, 1982.

[6] D.C. Groeneveld, S. Doerffer, R.M. Tain, N. Hammouda, S. Cheng, in: M. Giot, et al. (Eds.), Fluid-to-fluid Modelling of the Critical Heat Flux and Post-dryout Heat Transfer, Proceedings of the 4th World Conference on Experimental Heat Transfer, Fluid Mechanics and Thermodynamics vol. 2, Edizioni ETS, Pisa, 1997, pp. 859–866. Brussels, June 2-6, 1997.

[7] A.W. Bennett, G.F. Hewitt, H.A. Kearsey, R.K.F. Keeys, Heat transfer to steam-water mixtures flowing in uniformly heated tubes in which the critical heat flux has been exceeded 5373, UKAEA Report AERE – R, 1967.

[8] K.M. Becker, C.H. Ling, S. Hedberg, S. Strand, An Experimental Investigation of Post Dryout Heat Transfer, vol. 1, KTH-NEL-33, Stockholm, 1983, 2.

[9] K. Nishikawa, S. Yoshida, H. Mori, H. Takamatsu, An experiment on the heat transfer characteristics in the post-burnout region at high subcritical pressures, Nucl. Eng. Des. 74 (2) (1983) 233–239.

[10] S.K. Lee, S.H. Chang, Experimental study of post-dryout with R-134a upward flow in smooth tube and rifled tubes, Int. J. Heat Mass Tran. 51 (11–12) (2008) 3153–3163.

[11] K. Nishikawa, S. Yoshida, H. Mori, H. Takamatsu, Post-dryout heat transfer to Freon in a vertical tube at high subcritical pressures, Int. J. Heat Mass Tran. 29 (8) (1986) 1245–1251.

[12] M. Andreani, G. Yadigaroglu, Prediction methods for dispersed flow film boiling, Int. J. Multiph. flow 20 (1994) 1–51.

[13] J.C. Chen, A short review of dispersed flow heat transfer in post-dryout boiling, Nucl. Eng. Des. 95 (1986) 375–383.

[14] W.S. Hill, W.M. Rohsenow, Dryout Droplet Distribution and Dispersed Flow Film Boiling, 1982.

[15] H.Y. Jeong, H.C. No, Modelling for post-dryout heat transfer and droplet sizes at low pressure and low flow conditions, Int. Commun. Heat Mass Tran. 23 (1996) 767–778.

[16] R.A. Moose, E.N. Ganić, On the calculation of wall temperatures in the post dryout heat transfer region, Int. J. Multiphas. Flow 8 (1982) 525–542.

[17] A.F. Varone, W.M. Rohsenow, Post dryout heat transfer prediction, Nucl. Eng. Des. 95 (1986) 315–327.

[18] G.L. Yoder, W.M. Rohsenow, A solution for dispersed flow heat transfer using equilibrium fluid conditions, J. Heat Tran. 105 (1983) 10–17.

[19] H. Li, H. Anglart, CFD model of diabatic annular two-phase flow using the Eulerian–Lagrangian approach, Ann. Nucl. Energy 77 (2015) 415–424.

[20] H. Li, H. Anglart, Prediction of dryout and post-dryout heat transfer using a two-phase CFD model, Int. J. Heat Mass Tran. 99 (2016) 839–850.

[21] J. Shi, B. Sun, G. Zhang, F. Song, L. Yang, Prediction of dryout and post-dryout wall temperature at different operating parameters for once-through steam generators, Int. J. Heat Mass Tran. 103 (2016) 66–76.

[22] J. Shi, B. Sun, X. Yu, P. Zhang, F. Song, Modeling the full-range thermal-hydraulic characteristics and post-dryout deviation from thermodynamic equilibrium in once-through steam generators, Int. J. Heat Mass Tran. 109 (2017) 266–277.

[23] S. Torfeh, R. Kouhikamali, Numerical investigation of mist flow regime in a vertical tube, Int. J. Therm. Sci. 95 (2015) 1–8.

[24] H. Li, H. Anglart, Dryout prediction with CFD model of annular two-phase flow, Nucl. Eng. Des. 349 (2019) 20–26.

[25] J. Shi, B. Sun, Y. Chen, X. Yu, Y. Li, Influences of dryout parameters on dryout and post-dryout heat transfer, Int. J. Heat Mass Tran. 130 (2019) 901–911.

[26] D. Yu, L. Koeckert, F. Feuerstein, X. Cheng, Verification of proposed post-dryout heat transfer model, in: Conference Proceeding: 49th Annual Meeting on Nuclear Technology (AMNT 2018), 2018.

[27] L.S. Tong, Y.S. Tang, Boiling Heat Transfer and Two-phase Flow, CRC Press, 1997.

[28] X. Cheng, U. Müller, Review on Critical Heat Flux in Water Cooled Reactors. Scientific Report FZKA 6825, Institut für Kern- und Energietechnik, Forschungszentrum Karlsruhe GmbH, 2003.

[29] M. Cumo, G. Ferrari, G.E. Farello, A Photographic Study of Two-phase Highly Dispersed Flows, Comitato Nazionale per l'Energia Nucleare, Rome, 1971.

[30] D. Yu, Analysis and Modelling of Full-Range Post-Dryout Heat Transfer in Vertical Tubes, Diss, Karlsruhe Institute of Technology, 2019.

[31] G. Hadaller, S. Banerjee, Heat transfer to superheated steam in round tubes, AECL Rep (1969).

[32] R.P. Forslund, W.M. Rohsenow, Thermal Non-equilibrium in Dispersed Flow Film Boiling in a Vertical Tube, 1966.

[33] G.A. Hughmark, Mass and heat transfer from rigid spheres, AIChE J. 13 (1967) 1219–1221.

[34] J.C. Chen, F.T. Ozkaynak, R.K. Sundaram, Vapor heat transfer in post-CHF region including the effect of thermodynamic non-equilibrium, Nucl. Eng. Des. 51 (1979) 143–155.

[35] K.J. Liesch, G. Raemhild, K. Hofmann, Zur Bestimmung des Wärmeüberganges und der kritischen Heizflächenbelastung im Hinblick auf besondere Verhältnisse in den Kühlkanälen eines DWR bei schweren Kühlmittelverlustunfällen, Laboratorium für Reaktorregelung und Anlagensicherung (1975).